Article

Exploring the Stability Limits of Actin and Its Suprastructures

Christopher Rosin,[1] Mirko Erlkamp,[1] Julian von der Ecken,[2] Stefan Raunser,[2] and Roland Winter[1,*]
[1]Physical Chemistry I-Biophysical Chemistry, Department of Chemistry and Chemical Biology, TU Dortmund University, Dortmund, Germany; and [2]Department of Structural Biochemistry, Max Planck Institute of Molecular Physiology, Dortmund, Germany

ABSTRACT   Actin is the main component of the microfilament system in eukaryotic cells and can be found in distinct morphological states. Global (G)-actin is able to assemble into highly organized, supramolecular cellular structures known as filamentous (F)-actin and bundled (B)-actin. To evaluate the structure and stability of G-, F-, and B-actin over a wide range of temperatures and pressures, we used Fourier transform infrared spectroscopy in combination with differential scanning and pressure perturbation calorimetry, small-angle x-ray scattering, laser confocal scanning microscopy, and transmission electron microscopy. Our analysis was designed to provide new (to our knowledge) insights into the stabilizing forces of actin self-assembly and to reveal the stability of the actin polymorphs, including in conditions encountered in extreme environments. In addition, we sought to explain the limited pressure stability of actin self-assembly observed *in vivo*. G-actin is not only the least temperature-stable but also the least pressure-stable actin species. Under abyssal conditions, where temperatures as low as 1–4°C and pressures up to 1 kbar are reached, G-actin is hardly stable. However, the supramolecular assemblies of actin are stable enough to withstand the extreme conditions usually encountered on Earth. Beyond ~3–4 kbar, filamentous structures disassemble, and beyond ~4 kbar, complete dissociation of F-actin structures is observed. Between ~1 and 2 kbar, some disordering of actin assemblies commences, in agreement with in vivo observations. The limited pressure stability of the monomeric building block seems to be responsible for the suppression of actin assembly in the kbar pressure range.

INTRODUCTION

Actin is a substantial protein in nearly all eukaryotic cells and consists of 375 amino acids in the skeletal muscle isoform, α-actin (Fig. 1) (1). Actin can be found in at least two distinct morphological states in vivo: the monomeric state (globular (G)-actin) and the polymeric state (filamentous (F)-actin). By raising the ionic strength, G-actin spontaneously polymerizes into long helical filaments, which play a crucial role in important cellular processes such as muscle contraction, endocytosis, cytokinesis, cell locomotion, organelle transport, and generation of force (2). With increasing concentration of divalent ions, such as Mg^{2+}, or in the presence of actin-bundling proteins (e.g., Fascin, Espin, and α-actinin), parallel F-actin rods align axially with uniform polarity to assemble in highly organized, supramolecular structures called actin bundles (3). These larger structures are generally involved in protecting eukaryotic cells against mechanical stress. Cellular protrusions such as filopodia and microvilli are also invigorated by the formation of actin bundles (4).

F-actin is a highly dynamic assembly that can be affected by numerous factors, such as actin binding proteins, that enable the disassembly, elongation, branching, stabilization, destabilization, and shrinking of filaments (2). The dynamics and stability of G-actin and F-actin also depend on

the phosphorylation state of the bound nucleotide and on divalent cations (5). F-actin exhibits a higher temperature stability compared with G-actin, and it is thought that the thermal stability depends on the bound nucleotide and divalent cation. Furthermore, actin-binding proteins, such as profilin, also influence the thermal stability of the protein (6).

Although it is often forgotten, the greatest portion of our biosphere is in the realm of environmental extremes, including not only low and high temperatures but also high-pressure conditions (7). Although high hydrostatic pressure (HHP) significantly influences the structural properties and thus the functional characteristics of cells, this has not prevented life from invading the cold, high-pressure habitats of the deep sea (the average pressure on the ocean floor is ~400 bar). Deep-sea sediments and hydrothermal vents are densely crowded with barophilic-thermophilic species, and psychrophilic-barophilic bacteria are even found on the deepest ocean floor (at depths of 11,000 m) in the Mariana Trench, where pressures up to the 1 kbar level prevail. However, the adaptation mechanisms involved in the response to such stress conditions and the effect of HHP on biomolecular systems in general are still largely terra incognita (7,8).

Moreover, HHP has increasingly been used as a physical parameter in recent years to help delineate the free-energy landscape of biomolecules and elucidate which features and thermodynamic parameters are essential for determining their stability. For example, studies of proteins under

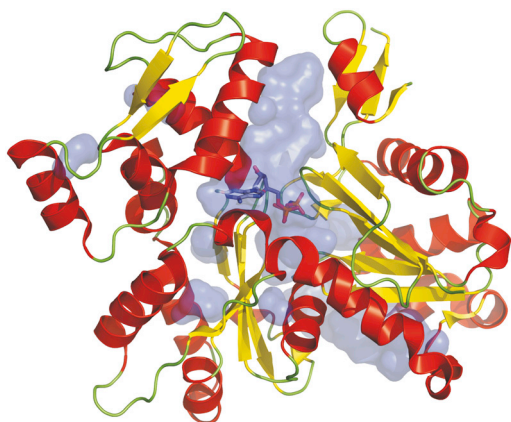http://dx.doi.org/10.1016/j.bpj.2014.11.006

CrossMark

FIGURE 1 3D ribbon model of the crystal structure of G-actin with bound ATP and internal cavities (PDB entry: 1NWK). Internal pockets (concave caverns with constrictions at the opening on the surface region, which allow easy access of water probes from the bulk) and voids (buried unfilled space inside the protein, which is inaccessible to water molecules) are marked in blue. The calculated overall pocket and void volume amounts to ~1.1% of the total molar volume (8) of the protein. The calculated void volume contributes to 0.075% to the molar volume of the protein. To see this figure in color, go online.

pressure have revealed the magnitudes of volume and compressibility changes that accompany alterations in protein structure, and these data have been very important in developing theories about the factors that stabilize the native structure of proteins. In addition, such studies provided additional information about the types of bonding events and energy changes that are instrumental in stabilizing proteins (8,9).

In the past, investigators have largely studied the effects of pressure on rather simple biomolecular systems, such as lipid bilayers and monomeric proteins (9–13). For example, it was shown that a densely packed protein structure exhibiting only a few small cavities resulting from imperfect packing, a minimal hydrophobic solvent-accessible surface area, a reduced amount of ion pairs within or between residues or subunits, or stacking effects between aromatic amino acids leads to high-pressure stability (7). Pressure studies on more complex biomolecular systems and reactions, such as metabolic and signaling processes and polymerization reactions, are still very rare. In fact, next to pressure effects on lipid bilayer membranes, polymerization reactions (e.g., actin polymerization) have been found to be among the most pressure-sensitive events encountered so far (14–19). In 1966, Ikkai and Ooi (18) explored the effects of pressure on the stability of actin. They showed that G-actin is more pressure sensitive than F-actin, and concluded that pressure shifts the equilibrium of the G-to-F transformation toward the monomeric state of the protein. They also found that ATP-bound actin is more pressure stable than ADP-actin, and that Mg^{2+} ions seem to have a higher protective effect than Ca^{2+} (18). In 1985, Swezey and Somero (16) analyzed and compared the effects of pres-

sure on different α-actin isoforms of organisms living at different temperatures and pressures as their usual habitat. They found that volume changes of F-actin upon pressurization are larger for organisms living under ambient pressure conditions compared with deep-sea organisms. Ikeuchi et al. (15) calculated the volume change of G-actin and F-actin upon unfolding to be −72 and −67 mL mol^{-1}, respectively, indicating a similar dense packing of the proteins.

In this study, we set out to quantitatively explore the structure and stability of G-actin, F-actin, and bundled (B)-actin over a wide range of temperatures and pressures to establish a temperature- and pressure-stability diagram of the different actin structures and polymorphs. Our goal was to gain a mechanistic understanding of the limitations of these temperature and pressure stabilities, and hence elucidate the limited pressure stability of actin assemblies observed in vivo.

MATERIALS AND METHODS

Materials and sample preparation

α-Actin and Cys374-labeled tetramethylrhodamine (TMR)-α-actin were purchased from HYPERMOL (Bielefeld, Germany). As G-actin is also able to polymerize at high protein concentrations (above ~5 mg mL^{-1}) in the absence of high ionic strength, Cys374-labeled TMR-G-actin was used to inhibit the G-to-F transformation in control studies (20). Fourier transform infrared (FTIR) spectroscopy and small-angle x-ray scattering (SAXS) measurements on TMR-α-actin were performed in 50 mM Tris-Cl, pH 8.6, 10 mM ATP, 2.4 mM dithiothreitol (DTT), 2 mM CaCl$_2$, 1 mM NaN$_3$. F-actin measurements were obtained in a buffer consisting of 50 mM Tris-Cl, 10 mM imidazole, pH 7.8, 10.6 mM ATP, 2 mM CaCl$_2$, 2 mM MgCl$_2$, 100 mM KCl, 2.4 mM DTT, 1 mM NaN$_3$. Bundling of polymerized actin filaments was induced via addition of 50 mM MgCl$_2$ to F-actin solutions. Calorimetric measurements on G-actin were carried out in a low-ionic-strength buffer containing 2 mM Tris-Cl, pH 8.6, 0.4 mM ATP, 0.08 mM CaCl$_2$, 0.1 mM DTT, 1 mM NaN$_3$. For calorimetric, transmission electron microscopy (TEM), and laser scanning confocal microscopy (LCSM) measurements on F- and B-actin, we employed the same buffer conditions as used in the FTIR experiments. For LCSM experiments, actin samples were stained with phalloidin-TMR B isothiocyanate (Sigma-Aldrich, Seelze, Germany) after the pressurization/heating procedure.

Temperature- and pressure-dependent FTIR spectroscopy

Temperature-dependent FTIR measurements were performed using a Nicolet 5700 (Thermo Fisher Scientific, Waltham, MA) equipped with a liquid-nitrogen-cooled MCT detector (HgCdTe) in the wavenumber range of 4000–1100 cm^{-1}. A sample volume of ~20 μL was placed between two CaF$_2$ windows separated by a mylar spacer (thickness, 50 μm; effective sample volume, 3.9 μL) and assembled in a temperature cell. To make sure that the sample was equilibrated, each temperature was maintained for 12 min before spectra were collected.

Pressure-dependent FTIR spectra were collected in a MAGNA 550 (Thermo Fisher Scientific) equipped with a liquid-nitrogen-cooled MCT detector (HgCdTe) within 4000–650 cm^{-1}. To achieve pressures up to 16 kbar, a membrane-driven diamond anvil cell (Diacell VivoDAC; Almax easyLab), equipped with an automated pneumatic pressure controller (Diacell iGM Controller; Almax easyLab, Diksmuide, Belgium), was used. For the high-pressure FTIR experiments, a 50-μm-thick gasket made of

brass with a 0.5 mm drilled opening (effective sample volume 9.8 nL) was placed onto a 730-μm-thick Type IIa diamond window (Almax easyLab). For accurate determination of the pressure in the sample, the pressure dependence of the SO_4^{2-} stretching mode of $BaSO_4$ was used as an internal pressure gauge [21].

For all FTIR experiments, a protein concentration of 25 mg mL^{-1} was used. The temperature was controlled via an external water bath. The temperature was measured with a digital thermometer placed in the sample cell (accuracy: $\pm 0.5°C$), with a controllable temperature range of 1–98°C, and the sample chamber was continuously purged with CO_2-free and dry air. For each temperature or pressure, a single spectrum was obtained by collecting and averaging 256 spectra in a row with the use of the Omnic 7.2 spectral processing software, and was apodized by a Happ-Genzel function. Spectra were processed and analyzed with Thermo Grams 9.1 software as follows: After buffer subtraction and smoothing, the area of the amide I' band (1700–1600 cm^{-1}) was normalized. To reveal the number of subbands and detect conformational changes, second derivative, Fourier self-deconvoluted, and difference spectra were analyzed. The amide I' band region of G-, F-, and B-actin was decomposed into eight underlying subbands, and the underlying secondary structure element was determined using mixed Gaussian-Lorentzian lineshape functions in the fitting procedure (Table S1 in the Supporting Material) [22].

Assuming a two-state unfolding or dissociation process of the protein, a Boltzmann function can be fitted to the temperature- and pressure-dependent sigmoidal curve progression of the secondary structural elements. The temperature- and pressure-induced intensity changes are given by

$$I = \frac{I_1 - I_2}{1 + e^{-(1/T_m - 1/T) \cdot (\Delta H/R)}} + I_2 \tag{1}$$

and

$$I = \frac{I_1 - I_2}{1 + e^{-(p - p_m) \cdot (\Delta V/RT)}} + I_2, \tag{2}$$

where I_1 and I_2 are the plateau values of the IR band intensities of the folded and unfolded/dissociated protein, respectively. The inflection points of the sigmoidal curves are described by T_m and p_m (the transition temperature and pressure, respectively). The thermodynamic parameters ΔH and ΔV are the standard enthalpy and volume changes of the reaction, respectively, and can be directly determined from the fits to the experimental data.

Differential scanning calorimetry and pressure perturbation calorimetry

All calorimetric experiments were conducted using a MicroCal (Northampton, MA) VP-DSC system equipped with a pressure perturbation calorimetry (PPC) pressurizing accessory. The volume of the sample and reference cells was ~0.5 mL. The sample cell was filled with the protein solution, and the reference cell contained the corresponding buffer solution. For differential scanning calorimetry (DSC) measurements, a protein concentration of 1.2 mg mL^{-1} was measured at 20–90°C, with a heating rate of 30°C h^{-1}. PPC measurements were performed using a protein concentration of 4 mg mL^{-1} and pressure jumps of 5 bar using N_2 in a temperature range from 5°C to 90°C. For each sample, a set of reference measurements of the corresponding buffer versus buffer, buffer versus water and water versus water was collected. Using MicroCal Origin processing software, we fitted and analyzed the DSC and PPC thermograms. From the DSC data, we obtained the temperature-dependent heat capacity changes, Δc_p, the calorimetric enthalpy change, ΔH_{cal}, and the transition temperature, T_m. The PPC data yield the temperature dependence of the coefficient of thermal expansion, $\alpha(T)$, and the relative volume change, $\Delta V/V$ (see Eq.

3), upon phase changes by integrating over the peak area in the temperature interval from T_1 to T_2 [23]:

$$\frac{\Delta V}{V} = \int_{T_1}^{T_2} \alpha(T) dT. \tag{3}$$

EM

Each sample of freshly prepared F-actin or B-actin (4 μL) was adsorbed on glow-discharged carbon grids before negative staining with 0.75% uranyl formate as previously described [24]. Prepared specimens were screened on a JEOL JEM-1400 electron microscope (Peabody, MA) equipped with an LaB$_6$ filament and operated at 120 kV. Images were recorded on a TVIPS TemCam-F416 CMOS camera. To be able to pressurize the actin samples up to 5 kbar before transferring them to the electron microscope, we constructed a new high-pressure autoclave. The outer metal vessel was tooled from the nickel-based alloy Allvac 718 and allowed pressurization of the fluid samples up to 5 kbar at ambient temperature. As the sample container, we used a Teflon cylinder with a small-bore hole for adding the sample solution (sample volume: 30 μL). The sample solution was separated by a thin polymer membrane from the pressurized medium (water). F-actin (1 mg mL^{-1}) was pressurized/heated in 50 mM Tris-Cl, 10 mM imidazole, pH 7.8, 10.6 mM ATP, 2 mM CaCl$_2$, 2 mM MgCl$_2$, 100 mM KCl, 2.4 mM DTT, 1 mM NaN$_3$. Bundling of polymerized actin filaments was induced via addition of 50 mM MgCl$_2$ to F-actin (0.5 mg mL^{-1}) solutions before pressurization/heating. After pressurization/heating, the samples were immediately placed on ice. For subsequent EM studies, the final concentration was adjusted empirically.

CLSM

For fluorescence microscopy measurements, samples were stained after pressurization/heating (see the previous paragraph) using phalloidin. CLSM measurements were performed on a Nikon Eclipse TE300 inverted microscope (Melville, NY) equipped with a Biorad MRC1024 confocal imaging system (Hercules, CA). Fluorescence was excited by the 568 nm line of a krypton argon laser. A water immersion objective (Nikon Plan Apo 60×/1.2) was used to focus the laser beam onto the sample.

SAXS measurements

SAXS measurements were carried out on a SAXSess instrument (Anton Paar, Graz, Austria) using a monochromatic x-ray beam ($\lambda = 1.54$ Å) with line focus and an imaging plate as detector. Scattering patterns were collected over 30 min per image. They were processed and analyzed using the PCG software package developed by O. Glatter (University of Graz; Anton Paar) [25]. A protein concentration of 10 mg mL^{-1} was used.

Measurement of pocket and void volumes

Pocket and void volumes were calculated using the CASTp server [26]. Voids are defined as buried empty spaces within the protein interior that are inaccessible to water molecules. Pockets are defined as concave cavities with constrictions at the opening on the surface region of the protein, which are easily accessible to water molecules. Pockets and voids were modeled by a spherical probe for H_2O with a diameter of 1.4 Å. The contribution of pockets and void volumes to the overall molar volume was calculated using molar volumes of 32,200 mL mol^{-1} (G-actin) and 31480 mL mol^{-1} (F-actin), respectively [27]. All calculations for G-actin were based on the PDB structure 1NWK [28], and those for F-actin were based on PDB 3G37 [29]. The atomic model of G-actin was visualized using PyMOL [30].

RESULTS AND DISCUSSION

To gain a deeper insight into the temperature- and pressure-dependent structure and phase behavior of monomeric actin (G-actin), F-actin, and B-actin, we used FTIR spectroscopy, DSC, PPC, SAXS, LCSM, and EM, covering a wide range of temperatures and pressures (from 5°C to 90°C and from 1 bar to 15 kbar (15 GPa), respectively). The FTIR spectroscopy data allowed us to detect changes in secondary structural elements via changes in hydrogen (H)-bonding patterns and to derive associated thermodynamic parameters, such as changes in enthalpy, entropy, and volume, upon phase transformations. The calorimetrical methods we used (DSC and PPC) provide additional thermodynamic information under ambient pressure conditions, and volumetric and hydrational changes upon protein unfolding and dissociation, respectively. To visualize morphological changes upon temperature and pressure perturbation, we used LCSM and TEM.

Effects of temperature and pressure on monomeric actin

Fig. 2, aA–aD, display examples of temperature- and pressure-dependent FTIR spectra, as well as the population of different secondary structural elements of G-actin as a function of temperature and pressure. Fig. 2 aC shows the changes that occurred in the deconvoluted amide I' band of G-actin while pressure was increased (at $T = 50°C$), and Fig. 2 aD depicts the influence of temperature on structural changes of the protein at ambient pressure. In both cases, the mainly affected secondary structural elements of the protein are α-helices (which absorb at a wavenumber of ~1655 cm^{-1}), intramolecular β-sheets (which absorb at ~1635 cm^{-1} and ~1627 cm^{-1}), and intermolecular β-sheets (with aggregation bands appearing at 1616 cm^{-1} and 1685 cm^{-1}) (Table S1). The crystal structure of monomeric rabbit skeletal muscle α-actin in the ATP-bound state exhibits a helical amount of 41% and a β-sheet content of 20% (28). Our FTIR analysis shows a very similar amount of helical structures (~40%). The β-sheet content is a bit higher compared with that observed in the crystal structure, which is probably due to the slightly different absorption coefficients of the different secondary structures; however, this is not important, as we discuss relative changes only. With increasing temperature or pressure, the population of α-helices and intramolecular β-sheets at 1627 cm^{-1} decreases, but temperature and pressure have different effects on the population of the intramolecular sheets that appear at ~1635 cm^{-1}.

Between 20°C and 50°C, no significant changes in the native structure of G-actin are observed (Fig. 2, aA and aB). Beyond $T \approx 50°C$, thermal unfolding of G-actin takes place, accompanied by decreasing amounts of α-helices (~−14%) and intramolecular β-sheets (~−4%). Upon tem-

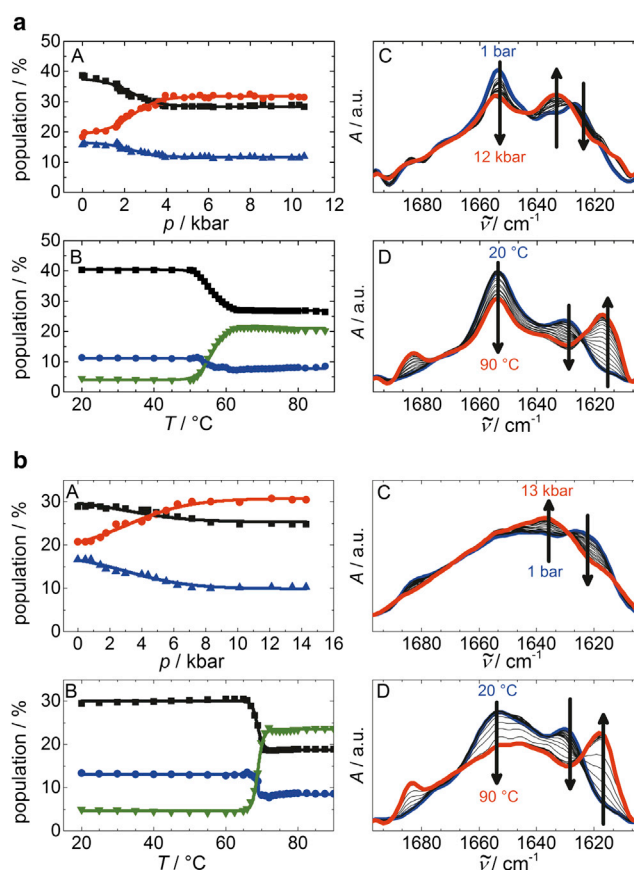FIGURE 2 (a and b) Temperature- and pressure-dependent FTIR data for (a) G-actin and (b) B-actin. (A and B) Changes in secondary structure elements by pressure at a selected temperature (A) and temperature-dependent changes at ambient pressure (B). (C and D) Example of pressure- (C) and temperature- (D) dependent changes in the deconvoluted absorption signal of the amide I' band (see Supporting Material for additional data). Lines are Boltzmann fits to the experimental data using Eqs. 1 and 2. Black box, α-helix (1655 cm^{-1}); red circle, intramolecular β-sheets (1635 cm^{-1}); blue up triangle, intramolecular β-sheets (1627 cm^{-1}); green down triangle, intermolecular β-sheets (1616 cm^{-1}). To see this figure in color, go online.

perature-induced unfolding of the protein, antiparallel intermolecular β-sheets are formed (~+16%) (with IR signatures at 1685 cm^{-1}/1616 cm^{-1}), indicating aggregation of the protein (Fig. 2 aD). Boltzmann fits to the experimental data (Eq. 1) yield an unfolding temperature, T_m, of 56°C ± 2°C and a van't Hoff enthalpy change, ΔH_{vH}, of 483 ± 101 kJ mol^{-1} for the transition. Because heat-induced protein unfolding and subsequent aggregation is an irreversible process, the thermodynamic data have to be considered with care, but may serve for comparison with the ΔH_{vH}-values for B- and F-actin (31–33).

With increasing pressure, the population of intramolecular sheets at 1635 cm^{-1} increases, whereas the amount of β-sheets absorbing at 1627 cm^{-1} (indicating β-sheets with a stronger H-bonding pattern) decreases concomitantly upon compression. Analysis of the pressure-dependent FTIR data measured at temperatures between 5°C and

50°C yield unfolding pressures, p_u, between ~1 and ~2.5 kbar. The p_u-value of 2 kbar observed for $T = 20$°C is, within experimental error, in good agreement with fluorescence spectroscopy data reported by Ikeuchi et al. (15). Using Eq. 2, we determined the volume change upon unfolding, which amounts to -12 ± 9 mL mol^{-1} at 5°C, -16 ± 6 mL mol^{-1} at 20°C, and -45 ± 13 mL mol^{-1} at 50°C. As a mechanism for pressure-induced unfolding of proteins, the release of void volume, electrostrictive effects of newly exposed and hydrated charged and polar groups, and weakening of hydrophobic interactions are generally discussed (9). Since actin self-assembly is an entropy-driven process, this suggests a critical role for hydrophobic effects in actin polymerization, which are known to be weakened at high pressure (34).

The DSC thermograms of G-actin exhibit a broad peak between 48°C and 66°C, with a mean transition temperature, T_m, of ~59.5°C (Fig. 3 A), in good agreement with our FTIR results and literature data (6,35). Analysis of the DSC peak shape by application of Fourier self-deconvolution (FSD) functions suggests that the unfolding of G-actin is a biphasic unfolding process with transition temperatures appearing at 56.5°C and 60.3°C, respectively (Fig. 3 B), in agreement with previous findings (35). A subsequent DSC run of the same sample reveals that the thermal unfolding and subsequent aggregation of G-actin are irreversible. X-ray diffraction data show that G-actin consists of two major domains connected by a linker α-helix, with domains I (sub-

domains 1 and 2) and II (subdomains 3 and 4) building up a nucleotide-binding cleft (28). The biphasic unfolding behavior of G-actin is likely due to a sequential unfolding process of the two domains, which are divided by a cleft, as proposed by Bertazzon et al. (36). Integration of the overall transition peak results in a calorimetric enthalpy change, ΔH_{cal}, of 364 ± 34 kJ mol^{-1}, which is slightly smaller than the spectroscopically determined van't Hoff value, ΔH_{vH}, based on a simple two-state transition model. Supplemental SAXS experiments on our sample (Fig. S1) reveal the existence of small populations of dimers or trimers, which could also contribute to the width of the DSC peak at such relatively high concentrations.

Fig. 3 C depicts the temperature dependence of the coefficient of thermal expansion, α, of the three different actin structures. Using a partial molar volume of 0.749 mL g^{-1} (37) and a molecular mass of 42,348 Da for G-actin, the change in volume upon thermal unfolding can be determined. We obtain -36 ± 20 mL mol^{-1} by integrating $\alpha(T)$ over the transition region (defined by the more accurate DSC data), which constitutes ~0.1% of the total volume of the protein. Calculating the contributions of small empty cavities for G-actin yields ~0.075% (24 mL mol^{-1}) of the total molecular volume of the protein, which is very close to the measured ΔV-value (see also Fig. 1). However, the experimentally determined apparent volume change of unfolding may also contain hydrational contributions owing to changes in the solvent-accessible surface area.
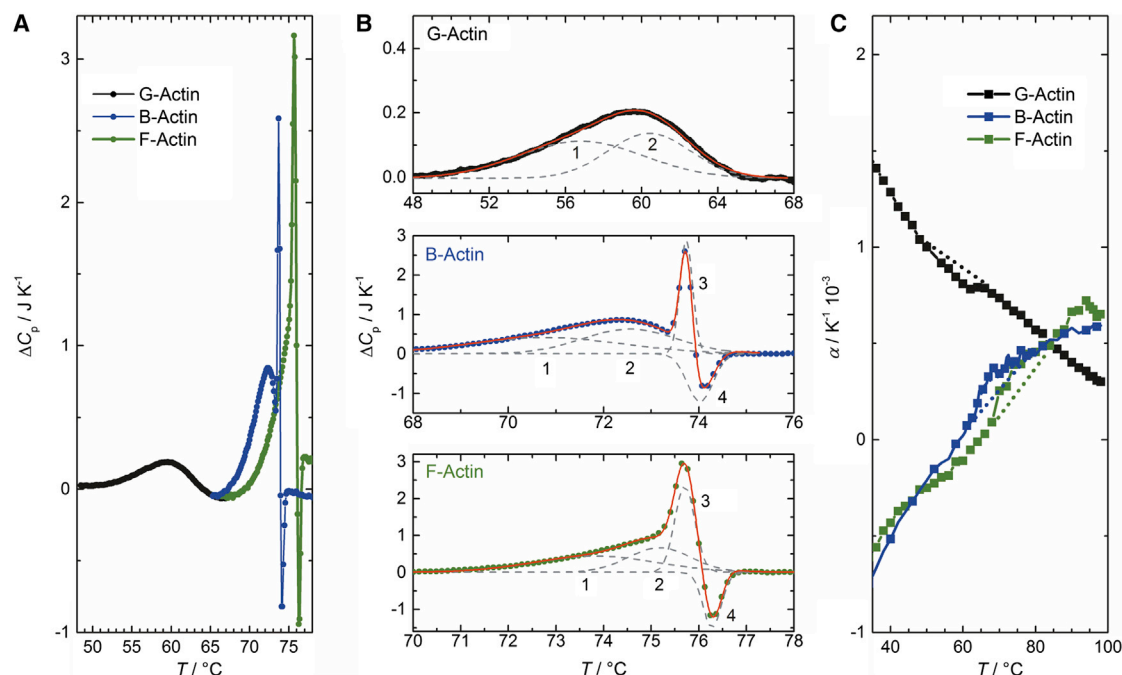

FIGURE 3 (A) Calorimetric studies of G-, B-, and F-actin. DSC thermograms (ΔC_p with respect to solvent) of the various actin structures display differences in thermal stability. (B) Deconvolution analysis of DSC peaks reveals a biphasic unfolding process for G-actin and a more complex triphasic behavior in the case of B- and F-actin. PPC measurements show temperature-dependent changes in the coefficient of thermal expansion. (C) Integrating the area of $\alpha(T)$ over the transition region yields the volume change of the transition at ambient pressure for the various actin species. To see this figure in color, go online.

Effects of temperature and pressure on B-actin

The folded state of actin bundles exhibits two main IR bands, at 1655 cm^{-1} (α-helices) and 1628 cm^{-1} (intramolecular β-sheets). The denatured state at 90°C shows essentially two β-sheet bands appearing at 1616 cm^{-1} and 1685 cm^{-1}, which are characteristic of aggregation of the protein. The structure analysis shows no significant change in secondary structures up to ~62.5°C (Fig. 2 bB). Between ~65°C and 72°C, a significant decrease of α-helices (~−11%) and intramolecular β-sheets (~−6%) takes place, indicating unfolding of the protomer structure. The population of intermolecular β-sheets increases concomitantly by ~19%.

Upon pressurization, α-helices (at 1653 cm^{-1}) and intramolecular β-sheets (at 1627 and 1635 cm^{-1}) are mostly affected (Fig. 2 b). However, changes in α-helix content decrease with increasing temperature and, interestingly, are absent at 60°C (Figs. 2 bC and S4). The population of intramolecular β-sheets at 1627 cm^{-1} decreases with increasing pressure at the expense of those absorbing at 1635 cm^{-1}. The transition pressures, p_u, range from 1.8 to 3.0 kbar for B-actin. The accompanying volume changes, ΔV, upon pressure-induced unfolding are very small. They vary between -9 ± 6 mL mol^{-1} at $T = 25°C$ and -26 ± 7 mL mol^{-1} at $T = 60°C$.

Hence, temperature- and pressure-induced unfolding is connected with a loss of α-helical structures and the stronger H-bonded β-sheets (absorbing at 1627 cm^{-1}). However, temperature and pressure have different effects on the weaker H-bonded intramolecular β-sheets (absorbing at 1635 cm^{-1}): compression increases the population of these β-sheets, whereas temperature has no significant impact.

A global fit to the experimental data yields an unfolding temperature of 68.9°C $\pm$ 2°C and a van't Hoff enthalpy change of 1120 $\pm$ 175 kJ mol^{-1}. The transition peak of B-actin obtained by DSC (Fig. 3 B) appears between 68°C and 76°C, and the overall endothermic calorimetric enthalpy change at ambient pressure, ΔH_{cal}, amounts to 946 $\pm$ 65 kJ mol^{-1}. The DSC peak may be deconvoluted into several subpeaks. DSC peaks 1 and 2 are located at 70.8°C and 72.5°C, respectively, and can be ascribed to partial unfolding of the actin monomers within the filament. The sharp peak at $T = 73.7°C$ (peak 3) is probably due to the highly cooperative dissociation of the actin bundles, which is followed by exothermic aggregation (peak 4). These data are in good agreement with the temperature-dependent FTIR experiments, i.e., the corresponding changes in secondary structural elements occur in the same temperature range. Integration of the expansivity (PPC) data (Fig. 3 C) reveals a positive volume change, ΔV, of 34 $\pm$ 20 mL mol^{-1} for the overall transition at T_m, which is ~0.13% of the total volume of the protein.

Effects of temperature and pressure on F-actin

The corresponding results of the temperature- and pressure-dependent FTIR studies on F-actin are similar to those ob-

tained for B-actin and are displayed in Fig. S3. Similar temperature- and pressure-dependent signatures are observed as for B-actin. Minor differences are only seen in the population of some secondary structure elements and in their temperature and pressure stability (compare Figs. S3 and S4). Between 70°C and 79°C, the heat-induced unfolding transition takes place, with T_m of 75.5 $\pm$ 2°C and ΔH_{vH} of 821 $\pm$ 141 kJ mol^{-1}. The pressure-dependent FTIR data show a decrease in the population of α-helices, an increase in intramolecular β-sheets at 1635 cm^{-1}, and a decrease in intramolecular β-sheets at 1627 cm^{-1} upon compression, in agreement with earlier qualitative results (38). Pressure-induced unfolding occurs between 3.3 and 4.1 kbar for temperatures ranging from 10°C to 60°C, and the corresponding volume changes are again very small, varying between -29 and -14 mL mol^{-1} for the different temperatures, indicating a tight packing of the filamentous polymer chain.

Similar DSC traces are observed for B- and F-actin (Fig. 3 B). Aggregation upon temperature-induced unfolding of F-actin was also shown by Levitsky et al. (39). The DSC data reveal a triphasic unfolding/dissociation scenario and an endothermic calorimetric enthalpy change, ΔH_{cal}, of 874 $\pm$ 36 kJ mol^{-1}, in good agreement with literature data (35). DSC peaks 1 (73.8°C) and 2 (75.2°C) are related to partial unfolding of the subunit of the monomer within the polymer chain, leading to a cooperative dissociation of the filament at ~75.7°C (peak 3), which is followed by exothermic aggregation at 76.3°C (peak 4). The latter process is also observed in the FTIR data, which show a strong increase in intermolecular β-sheets in the same temperature range (see Fig. S3). Using a molecular mass of 42.348 g mol^{-1} and a partial molar volume of 0.632 mL g^{-1} (37), the volume change, ΔV, is calculated to be 26 $\pm$ 20 mL mol^{-1} for $T = T_m$ at ambient pressure (~0.1% of the total volume of the protein). Calculation of the void volume of the filamentous actin resulted in 29 mL mol^{-1} (0.09% of the total volume of the protein), which is similar to the experimentally derived ΔV-value.

Comparison of G-actin, F-actin, and B-actin stability

The FTIR experiments reveal that with increasing temperature in G-actin, F-actin, and B-actin, the α-helices and intramolecular β-sheets decrease, whereas intermolecular β-sheets are formed upon unfolding, leading to nonfilamentous, amorphous aggregation of actin. Compared with G-actin, the population of α-helices decreases slightly upon formation of the supramolecular assemblies of F- and B-actin. For all actin polymorphs, heat-induced unfolding leads to such aggregation, whereas pressure-induced unfolding inhibits the aggregation process, a phenomenon that has also been observed for other amyloidogenic proteins (35,39–41). F-actin exhibits the highest unfolding temperature ($T_m = 75.5°C$), followed by B-actin ($T_m = 68.9°C$), and

finally G-actin with the lowest temperature stability (T_m = 56°C) (Table S2). B- and F-actin exhibit a triphasic unfolding process and larger transition enthalpies compared with G-actin, owing to additional energetically favorable protein-protein (intra- and interstrand) contacts within the filament and bundles. In the case of B- and F-actin, partial unfolding of the subunits is followed by a highly cooperative dissociation of the suprastructures, with subsequent amorphous aggregation of the unfolded monomer units. In the case of F-actin, each monomer within the filament is in contact with four adjacent monomers (42), leading in a higher enthalpy of unfolding, ΔH_{cal}, compared with the monomeric species (874 kJ mol^{-1} for F-actin versus 364 kJ mol^{-1} for G-actin). B-actin prepared at high Mg^{2+} concentrations is composed of filaments that are in close contact with each other and therefore exhibit additional protein-protein contacts, leading to still higher ΔH_{cal} and ΔH_{vH} values for the unfolding/dissociation process of B-actin.

We followed the pressure-dependent unfolding behavior of G-, B-, and F-actin by FTIR spectroscopy, which yields information about secondary structural changes and also enables one to calculate the unfolding pressures and changes in volume compared with the folded state of the protein at different temperature and pressure conditions. Fig. 4 shows a p,T-stability diagram of the various actin structures. It can be clearly seen that G-actin is not only the least temperature-stable but also the least pressure-stable species. In the temperature range between 5°C and 35°C, monomeric G-actin unfolds at pressures between 1 and 2.3 kbar. B-actin is more pressure stable than G-actin and, surprisingly, F-actin exhibits the highest pressure stability (as high as ~4 kbar at ambient temperatures). Pressure-induced volume changes upon unfolding, ΔV (Table S2), at the various temperatures are negative (in accordance with Le Châtelier's principle) and, surprisingly, similar for all actin structures. The volume changes are generally very small, indicating compact pack-

ing of amino acids not only in G-actin but also in the supramolecular assemblies of actin. ΔV values range from about -10 to -45 mL mol^{-1} (i.e., on the order of only a few water molecules ($V(H_2O)$ = 18 mL mol^{-1})). Hence, the size and number of the cavities or packing defects, which are considered to be major driving forces for pressure-induced unfolding of monomeric proteins (43,44), cannot be the only reason for the different pressure sensitivities of the three actin species. In addition, hydration differences (which are dependent on the chemical makeup and size of the solvent-accessible surface area) might play a role, and, even more likely, differences in pressure stability may be grounded in differences in intra- and interstrand interactions.

The FTIR data of the native species at 20°C indicate that G-actin consists of a slightly higher amount of α-helices (~1655 cm^{-1}) and slightly lower amount of β-sheets compared with F- and B-actin (Figs. 2 and S5). When G-actin is polymerized into F-actin, a right-handed helix is established in which one monomer comes in contact with four adjacent monomers (42), thereby fostering intermolecular contacts. As a result, stabilization appears to be driven by favorable enthalpy changes, leading to marked stabilization of F-actin compared with G-actin (e.g., to an increase in unfolding pressure of $\Delta p_u \approx 1.5$ kbar at 25°C, and in unfolding temperature at ambient pressure of ΔT_m(1 bar) $\approx$ 19.5°C), which is reflected in a 2.4-fold increase of ΔH_{cal} (Table S2). In the case of B-actin, this stabilizing effect is also increased compared with G-actin ($\Delta p_u \approx 0.4$ kbar at 25°C, ΔT_m(1 bar) $\approx$ 12.9°C), but is lower compared with F-actin. The higher temperature and pressure sensitivity of actin bundles compared with filaments could be due to some destabilizing intermolecular contacts when whole filaments become axially aligned. This is also reflected in the FTIR data. A comparison of the amide I′ bands of F- and B-actin indicates differences in secondary structure, in particular a ~5.5% decrease of α-helices when bundles are formed. Compared with the pressure-induced unfolding scenario, ΔV values are on the order of 30 mL mol^{-1} and positive for F- and B-actin at their much higher unfolding temperatures, T_m. This can be explained by the temperature dependence of the expansion coefficient of the respective unfolded and folded states of the protein, with the latter becoming smaller than that of the folded state at high temperatures. As a result, ΔV may even change sign at high temperatures, as has also been observed for monomeric proteins such as SNase and its mutations (43,44). In addition, the volume increase could also be due to formation of the aggregate structure following the unfolding process, which is not observed upon pressure-induced unfolding.

The different slopes of $\alpha(T)$ of G-actin compared with F- and B-actin indicate that these actin species have different hydrational properties (Fig. 5). It has been shown that the apparent expansion coefficient, α, largely depends on the hydration properties at the protein-water interface
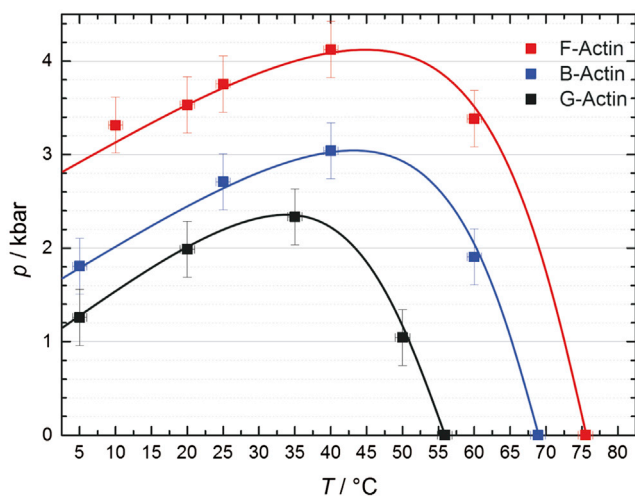

FIGURE 4 p,T-stability diagram of monomeric, bundled, and filamentous actin. To see this figure in color, go online.
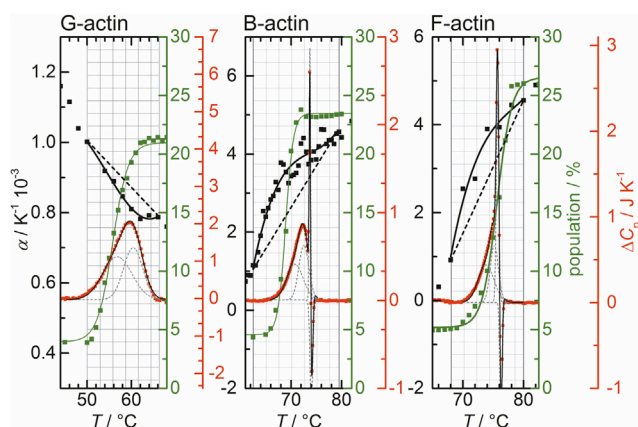
FIGURE 5 Comparison of the temperature-dependent spectroscopic and calorimetric results for each actin species. Changes in intermolecular β-sheet content (due to protein aggregation) as revealed by the FTIR data are shown in green. DSC data (ΔC_p with respect to solvent) are shown in red and underlying subbands are shown as dashed gray lines. The coefficient of isothermal expansion, α, measured by PPC, is plotted as black squares. To see this figure in color, go online.

(23,43–45). Generally, for highly charged and polar globular proteins, with a large preponderance of hydrophilic side chains and peptide groups relative to apolar groups at the protein-water interface, the α versus temperature behavior is characteristic of structure breakers, i.e., high α-values at low temperatures and a drastic decrease with increasing temperature. On the contrary, a positive slope of $\alpha(T)$ reflects an abundance of nonpolar residues (hydrophobic hydration) and/or an extended interstitial hydration layer network, which melts as temperature increases. The latter seems to be the case for F- and B-actin (Fig. 3 C). In fact, quasielastic neutron scattering experiments revealed that the hydration water around G-actin is more mobile than that around F-actin (46). Our conclusions would also be consistent with the negative values of the partial specific adiabatic compressibility of F-actin compared with G-actin (37).

To verify our conclusions regarding the temperature- and pressure-dependent morphological changes of actin assemblies, we performed TEM. Fig. 6 aA shows images of freshly prepared actin filaments. Nicely separated, long filaments can be seen, indicating the high quality of the purified sample. Pressurization of actin filaments leads to clearly visible (irreversible) morphological changes, which are depicted in Fig. 6, aB–aE. An increase in pressure up to 1.5 kbar leads to a disordering of the overall helical structure of actin filaments, in good agreement with literature data (47). The filaments shrink when pressure is increased up to 3 kbar. Upon pressurization up to 4 kbar, only a very few filaments can still be observed, and the majority of the remaining structures are monomers and small actin clusters. Pressurization of the sample up to 5 kbar leads to complete dissociation of actin filaments, in accordance with the high-pressure FTIR data. Heating of the sample at ambient

pressure up to 90°C results in the formation of large amorphous aggregates, again in good agreement with the conclusions drawn from the temperature-dependent FTIR data.

Fig. 6 bA shows an electron micrograph of freshly prepared actin bundles that assembled after the addition of 50 mM $MgCl_2$ to F-actin solutions. The bundles consist of axially aligned F-actin rods. Pressurization of the sample up to 0.5 kbar, 1.5 kbar (Fig. 6 bB), and 2.5 kbar (Fig. 6 bC) does not lead to significant morphological changes within the bundles. Dissociation of the bundles takes place above ~3.5 kbar (Fig. 6 bD). Upon pressurization up to 5 kbar, no bundles are observed and only a few small protein clusters are detected (Fig. 6 bE). Heating of the sample at ambient pressure shows the same effect as observed for filamentous actin, i.e., formation of large amorphous protein aggregates, in good agreement with the conclusions drawn from the temperature-dependent FTIR and DSC data.

CONCLUSIONS

Application of pressure to organisms living on Earth's surface generally leads to significant changes in the morphology and activity of their cells. In vivo studies have shown that high-pressure treatment leads to disruption of microtubules and depolymerization of F-actin (48–52), and the decrease of actin stress fibers is correlated with morphological changes in the cell shape (53). In the case of *Saccharomyces cerevisiae*, it was found that the organization of cytoskeletal structures is one of the most pressure-sensitive biochemical processes, and occurs upon pressurization up to ~1 kbar. At this pressure, actin structures located in buds and budding sites disappear, although some actin patches (smaller assemblies of actin filaments) remain (49). To gain a molecular-level understanding of the limited pressure stability of actin in vivo, we set out to evaluate the structure and stability of G-actin, F-actin, and B-actin over a wide range of temperatures and pressures.

Temperature-induced unfolding of F- and B-actin at ambient pressure leads to partial unfolding of the subunits, which is followed by a highly cooperative dissociation of the suprastructures and subsequent aggregation of the unfolded monomers. The much higher unfolding temperatures and larger transition enthalpies observed for F- and B-actin compared with G-actin reveal significant enthalpic stabilization of the actin suprastructures. Drastic differences between G-actin and F- and B-actin are also observed in the temperature dependence of the coefficient of thermal expansion. The positive slope of $\alpha(T)$ of F- and B-actin reflects the existence of an extended (also largely hydrophobic) and ordered interstitial hydration layer network, which is expected to help stabilize the supramolecular assemblies.

G-actin is not only the least temperature-stable but also the least pressure-stable species (order of stability: F-actin > B-actin > G-actin). Interestingly, an increased pressure sensitivity was also observed for monomeric capsid coat
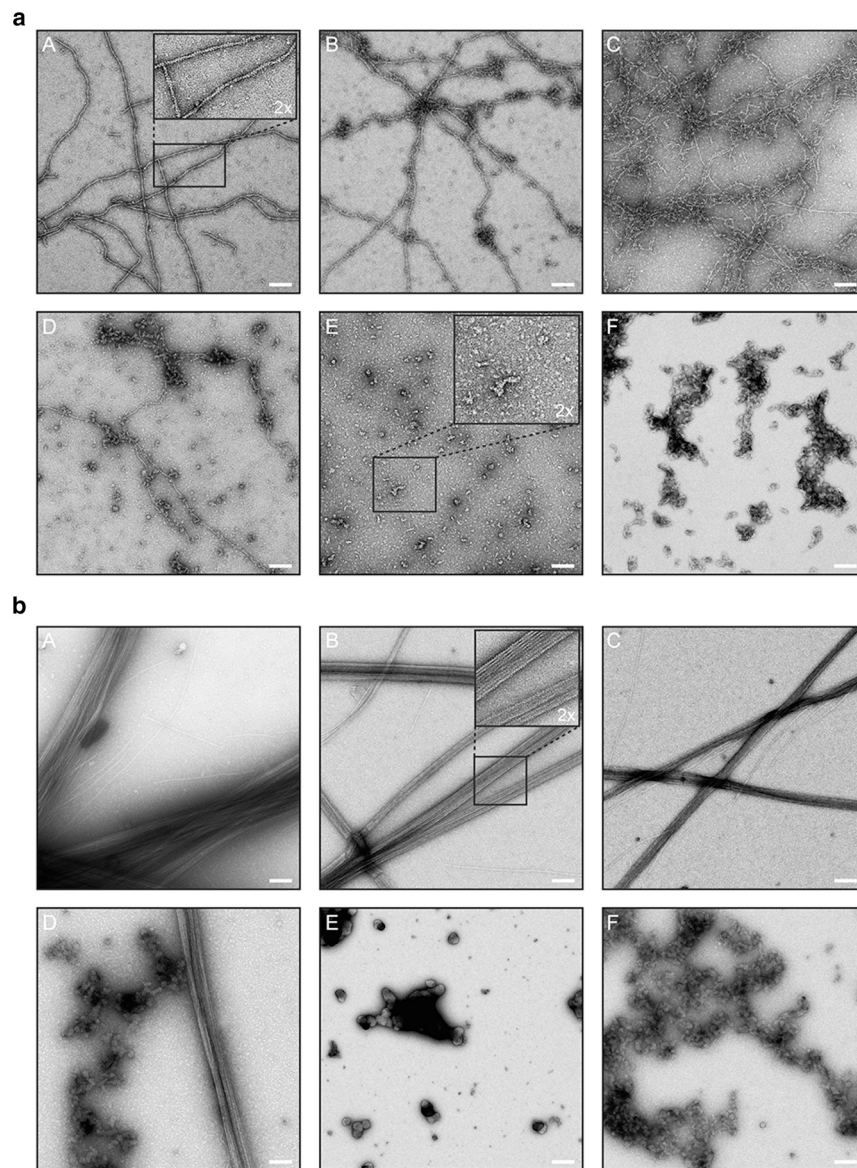
FIGURE 6 (*a*) Electron micrographs of pressurized/heated actin filaments. Samples were subjected to different pressures (for 20 min) followed by decompression and staining. (*A–E*) EM images of F-actin at 1 bar (*A*) and after pressurization up to 1.5 kbar (*B*), 3 kbar (*C*), 4 kbar (*D*), and 5 kbar (*E*). (*F*) To visualize the effect of temperature-induced aggregation, the sample was heated to 90°C for 20 min. Scale bars: 100 nm. (*b*) Electron micrographs of pressurized/heated actin bundles (B-actin). (*A–F*) EM micrographs of B-actin at 1 bar (*A*) and after pressurization up to 1.5 kbar (*B*), 2.5 kbar (*C*), 3.5 kbar (*D*), 5 kbar (*E*), and after heating up to 90°C for 20 min (*F*). Scale bars: 100 nm (*E*: 200 nm).

proteins, which exhibit a higher pressure stability when assembled into icosahedral virus particles (54–57). Significant differences in secondary structure elements have been observed for temperature- and pressure-induced unfolding. In particular, pressure-induced unfolding prohibits subsequent protein aggregation, since that is typically associated with an increase in system volume, whereas heat-induced unfolding is followed by irreversible aggregation in all cases. Upon pressure-induced unfolding, the population of α-helices decreases, and concomitantly (and in contrast to temperature-induced unfolding) the population of part of the intramolecular β-sheets increases upon compression.

The secondary structure of F-actin exhibits the highest pressure stability (as high as ~4 kbar at ambient temperature). Pressure-induced volume changes upon unfolding are very small, indicating compact packing of amino acids in this supramolecular assembly. Similar values are observed for B-actin. The ΔV-values range from about -10 to -45 mL mol^{-1}, i.e., on the order of a few water molecules only, and are even smaller than those typically observed for unfolding of most monomeric proteins (44). Interestingly, these values are on the same order of magnitude as those calculated for the void volume from the crystal structure data for F-actin ($V_{\mathrm{void}} \approx 29$ mL mol^{-1}). The size and number of cavities or packing defects are often considered to be among the major driving forces for pressure-induced unfolding of proteins. However, this does not explain the markedly different pressure sensitivities of the three actin species. As indicated by the combined thermodynamic data, enthalpic stabilization via intra- and interstrand interactions, including the formation of a stable extended hydration network, seems to contribute largely to the

stability of the supramolecular assemblies of actin. The secondary structures of actin bundles are slightly less temperature and pressure stable compared with filaments (Figs. 4 and S4). A higher piezo sensitivity of bundles compared with filamentous actin has also been suggested from in vivo observations (49). At sufficiently high pressures, between ~2 and 4 kbar, filamentous structures disassemble, and beyond ~4 kbar, complete dissociation of the supramolecular F-actin structures is observed in the EM micrographs. However, at much smaller pressures, between ~0.5 and 2 kbar, disordering of actin assemblies commences, in agreement with in vivo observations, revealing that the reorganization of disordered actin filaments is inhibited by pressures of ~1 kbar (49).

Compared with many other monomeric proteins, G-actin is a rather pressure-unstable protein (most monomeric proteins unfold between 4 and 10 kbar (7,58)). In deep-sea conditions, where temperatures as low as 1–4°C and pressures up to 1.1 kbar are reached, G-actin is hardly stable (see the p,T-stability diagram in Fig. 4). Its low stability is probably a consequence of its high flexibility, which is needed to enable easy rearrangement of its subunits upon initiation of the polymerization reaction (29,59). Conversely, F- and B-actin exhibit much higher temperature and pressure stabilities. Their supramolecular structures are also much more stable than nonfilamentous amorphous protein aggregates, which typically dissociate at a few hundred bars owing to their low packing density and large interstitial void volumes (8,58). The supramolecular assemblies of actin have sufficient temperature and pressure stability to be able to withstand the extreme conditions usually encountered on Earth. The limited pressure stability of their building block, G-actin, seems to be responsible for suppressing actin assembly in the kbar pressure range observed in vivo.

SUPPORTING MATERIAL

Six figures and two tables are available at http://www.biophysj.org/biophysj/supplemental/S0006-3495(14)01189-8.

REFERENCES

1. Sheterline, P., J. Clayton, and J. Sparrow. 1995. Actin. *Protein Profile.* 2:1–103.

2. Pollard, T. D., and J. A. Cooper. 2009. Actin, a central player in cell shape and movement. *Science.* 326:1208–1212.

3. Shin, H., and G. M. Grason. 2010. Structural reorganization of parallel actin bundles by crosslinking proteins: incommensurate states of twist. *Phys. Rev. E Stat. Nonlin. Soft Matter Phys.* 82:051919.

4. Claessens, M. M. A. E., C. Semmrich, …, A. R. Bausch. 2008. Helical twist controls the thickness of F-actin bundles. *Proc. Natl. Acad. Sci. USA.* 105:8819–8822.

5. Gaszner, B., M. Nyitrai, …, J. Belágyi. 1999. Replacement of ATP with ADP affects the dynamic and conformational properties of actin monomer. *Biochemistry.* 38:12885–12892.

6. Schüler, H., U. Lindberg, …, R. Karlsson. 2000. Thermal unfolding of G-actin monitored with the DNase I-inhibition assay stabilities of actin isoforms. *Eur. J. Biochem.* 267:476–486.

7. Gross, M., and R. Jaenicke. 1994. Proteins under pressure. The influence of high hydrostatic pressure on structure, function and assembly of proteins and protein complexes. *Eur. J. Biochem.* 221:617–630.

8. Meersman, F., I. Daniel, …, P. F. McMillan. 2013. High-pressure biochemistry and biophysics. *Rev. Mineral. Geochem.* 75:607–648.

9. Daniel, I., P. Oger, and R. Winter. 2006. Origins of life and biochemistry under high-pressure conditions. *Chem. Soc. Rev.* 35:858–875.

10. Panick, G., R. Malessa, …, C. A. Royer. 1998. Structural characterization of the pressure-denatured state and unfolding/refolding kinetics of staphylococcal nuclease by synchrotron small-angle X-ray scattering and Fourier-transform infrared spectroscopy. *J. Mol. Biol.* 275:389–402.

11. Zhai, Y., and R. Winter. 2013. Effect of molecular crowding on the temperature-pressure stability diagram of ribonuclease A. *ChemPhysChem.* 14:386–393.

12. Kapoor, S., G. Triola, …, R. Winter. 2012. Revealing conformational substates of lipidated N-Ras protein by pressure modulation. *Proc. Natl. Acad. Sci. USA.* 109:460–465.

13. Kapoor, S., A. Werkmüller, …, R. Winter. 2013. Pressure modulation of Ras-membrane interactions and intervesicle transfer. *J. Am. Chem. Soc.* 135:6149–6156.

14. Winter, R., and C. Jeworrek. 2009. Effect of pressure on membranes. *Soft Matter.* 5:3157–3173.

15. Ikeuchi, Y., A. Suzuki, …, C. Balny. 2002. Fluorescence study of the high pressure-induced denaturation of skeletal muscle actin. *Eur. J. Biochem.* 269:364–371.

16. Swezey, R. R., and G. N. Somero. 1985. Pressure effects on actin self-assembly: interspecific differences in the equilibrium and kinetics of the G to F transformation. *Biochemistry.* 24:852–860.

17. Ikkai, T., T. Ooi, and H. Noguchi. 1966. Actin: volume change on transformation of G-form to F-form. *Science.* 152:1756–1757.

18. Ikkai, T., and T. Ooi. 1966. The effects of pressure on F-G transformation of actin. *Biochemistry.* 5:1551–1560.

19. Kikumoto, M., Y. Tamura, …, K. Mihashi. 2003. Partial specific volume and adiabatic compressibility of G-actin depend on the bound nucleotide. *J. Biochem.* 133:687–691.

20. Dominguez, R., and P. Graceffa. 2003. Solution properties of TMR-actin: when biochemical and crystal data agree. *Biophys. J.* 85:2073–2074.

21. Wong, P. T. T., and D. J. Moffatt. 1989. A new internal pressure calibrant for high-pressure infrared spectroscopy of aqueous systems. *Appl. Spectrosc.* 43:1279–1281.

22. Panick, G., and R. Winter. 2000. Pressure-induced unfolding/refolding of ribonuclease A: static and kinetic Fourier transform infrared spectroscopy study. *Biochemistry.* 39:1862–1869.

23. Mitra, L., N. Smolin, …, R. Winter. 2006. Pressure perturbation calorimetric studies of the solvation properties and the thermal unfolding of proteins in solution—experiments and theoretical interpretation. *Phys. Chem. Chem. Phys.* 8:1249–1265.

24. Ohi, M., Y. Li, …, T. Walz. 2004. Negative staining and image classification—powerful tools in modern electron microscopy. *Biol. Proced. Online.* 6:23–34.

25. Fritz, G., A. Bergmann, and O. Glatter. 2000. Evaluation of small-angle scattering data of charged particles using the generalized indirect Fourier transformation technique. *J. Chem. Phys.* 113:9733–9740.

26. Binkowski, T. A., S. Naghibzadeh, and J. Liang. 2003. CASTp: Computed Atlas of Surface Topography of proteins. *Nucleic Acids Res.* 31:3352–3355.

27. Quirion, F., and C. Gicquaud. 1993. Changes in molar volume and heat capacity of actin upon polymerization. *Biochem. J.* 295:671–672.

28. Graceffa, P., and R. Dominguez. 2003. Crystal structure of monomeric actin in the ATP state. Structural basis of nucleotide-dependent actin dynamics. *J. Biol. Chem.* 278:34172–34180.

29. Murakami, K., T. Yasunaga, …, T. Wakabayashi. 2010. Structural basis for actin assembly, activation of ATP hydrolysis, and delayed phosphate release. *Cell.* 143:275–287.

30. The PyMOL Molecular Graphics System, Version 1.5.0.4 Schrödinger, LLC.

31. Herberhold, H., and R. Winter. 2002. Temperature- and pressure-induced unfolding and refolding of ubiquitin: a static and kinetic Fourier transform infrared spectroscopy study. *Biochemistry.* 41:2396–2401.

32. Panick, G., R. Malessa, and R. Winter. 1999. Differences between the pressure- and temperature-induced denaturation and aggregation of beta-lactoglobulin A, B, and AB monitored by FT-IR spectroscopy and small-angle X-ray scattering. *Biochemistry.* 38:6512–6519.

33. Smeller, L. 2002. Pressure-temperature phase diagrams of biomolecules. *Biochim. Biophys. Acta.* 1595:11–29.

34. Hummer, G., S. Garde, …, L. R. Pratt. 1998. The pressure dependence of hydrophobic interactions is consistent with the observed pressure denaturation of proteins. *Proc. Natl. Acad. Sci. USA.* 95:1552–1555.

35. Lorinczy, D., F. Könczöl, …, J. Belagyi. 1998. Structural stability of actin filaments as studied by DSC and EPR. *Thermochim. Acta.* 322:95–100.

36. Bertazzon, A., G. H. Tian, …, T. Y. Tsong. 1990. Enthalpic and entropic contributions to actin stability: calorimetry, circular dichroism, and fluorescence study and effects of calcium. *Biochemistry.* 29:291–298.

37. Suzuki, N., Y. Tamura, and K. Mihashi. 1996. Compressibility and specific volume of actin decrease upon G to F transformation. *Biochim. Biophys. Acta.* 1292:265–272.

38. Gicquaud, C., and P. Wong. 1994. Mechanism of interaction between actin and membrane lipids: a pressure-tuning infrared spectroscopy study. *Biochem. J.* 303:769–774.

39. Levitsky, D. I., A. V. Pivovarova, …, O. P. Nikolaeva. 2008. Thermal unfolding and aggregation of actin. *FEBS J.* 275:4280–4295.

40. Mishra, R., and R. Winter. 2008. Cold- and pressure-induced dissociation of protein aggregates and amyloid fibrils. *Angew. Chem. Int. Ed. Engl.* 47:6518–6521.

41. Lullien-Pellerin, V., and C. Balny. 2002. High-pressure as a tool to study some proteins' properties: conformational modification, activity and oligomeric dissociation. *Innov. Food Sci. Emerg. Technol.* 3:209–221.

42. dos Remedios, C. G., and P. D. J. Moens. 1995. Actin and the actomyosin interface: a review. *Biochim. Biophys. Acta.* 1228:99–124.

43. Roche, J., J. A. Caro, …, C. A. Royer. 2012. Cavities determine the pressure unfolding of proteins. *Proc. Natl. Acad. Sci. USA.* 109:6945–6950.

44. Frye, K. J., and C. A. Royer. 1998. Probing the contribution of internal cavities to the volume change of protein unfolding under pressure. *Protein Sci.* 7:2217–2222.

45. Zhai, Y., L. Okoro, …, R. Winter. 2011. Applications of pressure perturbation calorimetry in biophysical studies. *Biophys. Chem.* 156:13–23.

46. Fujiwara, S., M. Plazanet, and T. Oda. 2013. Coupling of the hydration water dynamics and the internal dynamics of actin detected by quasielastic neutron scattering. *Biochem. Biophys. Res. Commun.* 431:542–546.

47. Garcia, C. R. S., J. A. Amaral Júnior, …, S. Verjovski-Almeida. 1992. Dissociation of F-actin induced by hydrostatic pressure. *Eur. J. Biochem.* 209:1005–1011.

48. Sato, M., H. Kobori, …, M. Osumi. 1996. Schizosaccharomyces pombe is more sensitive to pressure stress than Saccharomyces cerevisiae. *Cell Struct. Funct.* 21:167–174.

49. Kawarai, T., S. Arai, …, M. Yamasaki. 2006. High-hydrostatic-pressure treatment impairs actin cables and budding in Saccharomyces cerevisiae. *J. Biosci. Bioeng.* 101:515–518.

50. Shimada, S., M. Andou, …, R. Hayashi. 1993. Effects of hydrostatic pressure on the ultrastructure and leakage of internal substances in the yeast Saccharomyces cerevisiae. *Appl. Microbiol. Biotechnol.* 40:123–131.

51. Kobori, H., M. Sato, …, M. Osumi. 1995. Ultrastructural effects of pressure stress to the nucleus in Saccharomyces cerevisiae: a study by immunoelectron microscopy using frozen thin sections. *FEMS Microbiol. Lett.* 132:253–258.

52. Abe, F., and K. Horikoshi. 2000. Tryptophan permease gene TAT2 confers high-pressure growth in Saccharomyces cerevisiae. *Mol. Cell. Biol.* 20:8093–8102.

53. Bourns, B., S. Franklin, …, E. D. Salmon. 1988. High hydrostatic pressure effects in vivo: changes in cell morphology, microtubule assembly, and actin organization. *Cell Motil. Cytoskeleton.* 10:380–390.

54. Da Poian, A. T., A. C. Oliveira, …, G. Weber. 1993. Reversible pressure dissociation of R17 bacteriophage. The physical individuality of virus particles. *J. Mol. Biol.* 231:999–1008.

55. Da Poian, A. T., J. E. Johnson, and J. L. Silva. 1994. Differences in pressure stability of the three components of cowpea mosaic virus: implications for virus assembly and disassembly. *Biochemistry.* 33:8339–8346.

56. Bispo, J. A. C., C. F. S. Bonafe, …, D. R. Norberto. 2012. Entropy and volume change of dissociation in tobacco mosaic virus probed by high pressure. *J. Phys. Chem. B.* 116:14817–14828.

57. Silva, J. L., A. C. Oliveira, …, D. Foguel. 2014. High-pressure chemical biology and biotechnology. *Chem. Rev.* 114:7239–7267.

58. Winter, R., D. Lopes, …, K. Vogtt. 2007. Towards an understanding of the temperature/ pressure configurational and free-energy landscape of biomolecules. *J. Non-Equilibrium Thermodyn.* 32:41–97.

59. Oda, T., M. Iwasa, …, A. Narita. 2009. The nature of the globular- to fibrous-actin transition. *Nature.* 457:441–445.